

# On Frequency-Dependent Dispersion Measures and the Extreme Scattering Events Toward PSR J2219+4754

M. T. Lam<sup>1,2</sup>, T. J. W. Lazio<sup>3</sup>, T. Dolch<sup>4</sup>, M. L. Jones<sup>1,2</sup>, M. A. McLaughlin<sup>1,2</sup>, D. R. Stinebring<sup>5</sup>, and M. Surnis<sup>1,2</sup>

<sup>1</sup> Department of Physics and Astronomy, West Virginia University, P.O. Box 6315, Morgantown, WV 26506, USA  
e-mail: michael.lam@mail.wvu.edu

<sup>2</sup> Center for Gravitational Waves and Cosmology, West Virginia University, Chestnut Ridge Research Building, Morgantown, WV 26505, USA

<sup>3</sup> Jet Propulsion Laboratory, California Institute of Technology, 4800 Oak Grove Drive, M/S 67-201, Pasadena, CA 91109, USA

<sup>4</sup> Department of Physics, Hillsdale College, 33 E. College Street, Hillsdale, Michigan 49242, USA

<sup>5</sup> Department of Physics & Astronomy, Oberlin College, Oberlin, OH 44074, USA

February 13, 2022

## ABSTRACT

*Context.* Variations in pulsar dispersion measures have been observed since shortly after the discovery of pulsars. As early as 2006, frequency-dependent dispersion measures have been observed and attributed to several possible causes. Cordes et al. (2016) demonstrated that ray-path averaging over different effective light-cone volumes through the turbulent ionized interstellar medium must contribute to this effect.

*Aims.* We assess the frequency-dependent dispersion measures and reported extreme scattering event(s) in Donner et al. (2019) seen in the direction of PSR J2219+4754 to determine if the observations are consistent with such an event.

*Methods.* We examine the observations of Donner et al. (2019) in the context of the recent literature on interstellar medium propagation effects and observations.

*Results.* We find that the frequency dependence of the dispersion measure timeseries for PSR J2219+4754 is consistent with being due solely to turbulence in the ionized interstellar medium and that there is no evidence for an extreme scattering event.

**Key words.** ISM: structure – pulsars: individual: PSR J2219+4754

## 1. Introduction

Donner et al. (2019, hereafter DVT+) have reported multi-year timing measurements of PSR J2219+4754 (B2217+47) and from those data have determined frequency-dependent variations in the dispersion measure (DM), or electron column density, along the line of sight. The authors conclude that the DM variations result from small-scale ( $\sim 1$  AU) structure in the interstellar medium (ISM). However, models of radio-wave propagation in the ISM developed by Cordes et al. (2016), in which the ISM is described by a power-law density function, show qualitatively similar variations.

While temporal DM variations have been observed for decades (Rankin & Roberts 1971; Phillips & Wolszczan 1991, 1992; Backer et al. 1993; Hobbs et al. 2004), frequency-dependent DM due to differing volumes of the ISM probed has only been observed more recently (Ramachandran et al. 2006, see also in Demorest 2007; Pennucci 2015). DVT+ most recently detected frequency-dependent DM in three-and-a-half years of timing of PSR J2219+4754 with three German stations of the International LOFAR (LOw-Frequency ARray) Telescope (ILT). A thorough treatment on the theory of frequency-dependent DM was given by Cordes et al. (2016). Ray-path averaging of the radio emission through different volumes, and therefore different electron content, of the turbulent ISM will result in a smoothing of the DM timeseries by a kernel that broadens rapidly at lower frequencies. The temporal variations

noted in the DM timeseries for PSR J2219+4754 by DVT+ for both the lower- and higher-frequency data qualitatively appear very similar to those predicted by Cordes et al. (2016), especially in that the higher radio-frequency DM data show higher fluctuation/Fourier-frequency structure than the lower radio-frequency timeseries. DVT+ conclude, however, that while the data are consistent with arising from the turbulent medium, multiple extreme scattering events (ESEs) have been observed both in the DM and in scattering measurements.

ESEs were originally seen as localized “events” in flux density measurements of compact radio sources (Fiedler et al. 1987; Cognard et al. 1993; Maitia et al. 2003). The first measurements of ESEs observed in DM and scintillation/scattering measurements were performed by Coles et al. (2015), describing ESEs observed towards two pulsars. DVT+ do not provide a timeseries of their scattering measurements, making a comparison to their DM timeseries, and to Coles et al. (2015), impossible.

In this work, we perform additional analyses on those performed by DVT+ and reinterpret the results. In §2, we reinterpret a structure-function analysis to show consistency of the frequency-dependent DM with a turbulent Kolmogorov medium. In §3, we further examine the purported ESE detection, analyzing the impact of a variety of timing effects on their results. We discuss the impact on precision pulsar-timing experiments in §4 and briefly discuss future observations of this type in §5. In the Appendix, we provide a derivation for DM estimation errors in the presence of time-of-arrival (TOA) uncertainties and

additional frequency-dependent time delays that is useful for a number of arguments in our work.

## 2. Structure Function Analysis

As part of their analysis, DVT+ (see their Figure 6) determine the structure function of the DM timeseries, defined as  $D_{\text{DM}}(\tau) = \langle [\text{DM}(t + \tau) - \text{DM}(t)]^2 \rangle$ , where  $\tau$  is the time lag separating two observations and the brackets denote the ensemble average. The authors find a power-law structure function with a spectral index consistent with that of Kolmogorov turbulence but do not report the actual spectral index (or range of spectral indices) resulting from the fit of the DM structure function. The fit was performed over lags  $\tau \leq 200$  days. However, the calculated structure function shows clear evidence of a white noise contribution at lags  $\tau \lesssim 30$  days. It is well known that a white noise contribution to a time series will produce a “plateau” at small lags (e.g., Cordes & Downs 1985) or for any trends (e.g., linear) in the data (Lam et al. 2016b; Jones et al. 2017) and bias the fit for the spectral index which will itself become a function of  $\tau$ ; the authors do not discuss the fitting of these features. For the purposes of this paper, we accept that a Kolmogorov (or near-Kolmogorov) spectrum is an acceptable fit to the DM structure function.

However, following the determination of a Kolmogorov spectrum, the authors then conclude that the cause of ESEs may not be “separate, localized events.” A spectrum steeper than Kolmogorov or discrete structures (or both) are required to produce canonical ESEs and the refractive effects observed in pulsar dynamic spectra (e.g., Roberts & Ables 1982; Hewish et al. 1985; Cordes & Wolszczan 1986; Romani et al. 1987); specifically, in a medium with a density spectrum having a power law form,  $P_{\delta n_e} \propto q^{-\beta}$ , these strong refractive effects occur for a density spectral index  $\beta > 4$ . Notably, DVT+ reference Fiedler et al. (1994) and Coles et al. (2015) as examples in which larger-scale turbulent structure is identified as the cause of the observed lensing; however, both of those works instead find the causes of their observations to be due to structures consistent with compact canonical ESEs. In the former, the authors examine the associated large-scale structure of the ISM in the foreground of sources with observed ESEs from Fiedler et al. (1987). In the latter, the “outer scale” of the ESE is taken to be of order the size scale of the smallest dimension of the lens, which is distinct from the outer scale of a Kolmogorov spectrum, which is known to be many orders of magnitude larger (Armstrong et al. 1995).

Using the constant value of the amplitude of the wavenumber spectrum they estimate,  $C_n^2 = 0.9 \times 10^{-3} \text{ m}^{-20/3}$ , and a distance estimate of 2.2 kpc from the NE2001 electron density model (Cordes & Lazio 2002), the corresponding scattering measure is  $\text{SM} = \int_0^{D_p} C_n^2(z) dz = 2.0 \times 10^{-3} \text{ kpc m}^{-20/3}$ , an order of magnitude higher than the value predicted by the NE2001 model<sup>1</sup>. Following Cordes et al. (2016, Eq. 6), the root-mean-square (rms) difference in DM between two spot frequencies  $\nu_1$  and  $\nu_2$ , where

$\nu_1 < \nu_2$ , for a uniform Kolmogorov medium is

$$\sigma_{\text{DM}(\nu)}(\nu_1, \nu_2) = 5.45 \times 10^{-6} \text{ pc cm}^{-3} F_{11/3}(r) \left( \frac{D_p}{1 \text{ kpc}} \right)^{5/6} \times \left( \frac{\nu_2}{1 \text{ GHz}} \right)^{-11/6} \left( \frac{\text{SM}}{10^{-3.5} \text{ kpc m}^{-20/3}} \right), \quad (1)$$

where the frequency ratio  $r \equiv \nu_2/\nu_1$ ,  $F_{11/3}(r)$  is a factor that contains all of the relative frequency dependence (Cordes et al. 2016, Eq. 11), and  $D_p$  is the pulsar distance. For frequencies at the centers of the two frequency bands from the observations of DVT+, we have  $\sigma_{\text{DM}(\nu)}(133 \text{ MHz}, 169 \text{ MHz}) = 0.6 \times 10^{-3} \text{ pc cm}^{-3}$ , while for the extremes of the bands,  $\sigma_{\text{DM}(\nu)}(118 \text{ MHz}, 190 \text{ MHz}) = 1.1 \times 10^{-3} \text{ pc cm}^{-3}$ . The bottom panel of Figure 5 of DVT+ shows rms variations at exactly these levels, suggesting that the observed frequency-dependent DM is consistent with being from a Kolmogorov medium.

## 3. ESE Interpretation

We disagree with the inference of multiple ESEs being responsible for the observed DM differences by DVT+. Qualitatively, the appearance of the DM time series is similar to that of other pulsars; for example, in the DM time series presented by Jones et al. (2017), one can identify similar features for PSR J0613–0200, PSR B1937+21, and potentially other pulsars in that dataset alone.

Additional evidence against these features being ESEs can be found by considering the expected DM amplitude. DVT+ identify the variation in DM between MJD 56950 and 57100 (their Figure 1) as an ESE by virtue of its amplitude  $|\delta\text{DM}| \approx 3 \times 10^{-3} \text{ pc cm}^{-3}$ . By considering the calculated structure function and relating that to the expected rms variations in the DM (Lam et al. 2016b, Eq. 30), we find

$$\begin{aligned} \sigma_{\text{DM}}(\tau) &= \left[ \frac{1}{2} D_{\text{DM}}(\tau) \right]^{1/2} \\ &= 1.2 \times 10^{-5} \text{ pc cm}^{-3} \left( \frac{\tau}{\text{day}} \right)^{5/6}. \end{aligned} \quad (2)$$

For  $\tau = 150$  days, then  $\sigma_{\text{DM}}(150 \text{ days}) = 0.8 \times 10^{-3} \text{ pc cm}^{-3}$ , and  $|\delta\text{DM}|$  is much larger than this rms variation.

If the DM variation is from a true steep gradient, then we can use an estimate of the rms DM gradient (rather than the rms DM, Lam et al. 2016b),

$$\sigma_{d\text{DM}/dt} \approx \frac{\sigma_{\text{DM}}(\tau)}{\tau}, \quad (3)$$

and compute the “signal-to-noise” ratio for such a gradient

$$R_{d\text{DM}/dt} \equiv \frac{|d\text{DM}/dt|}{\sigma_{d\text{DM}/dt}}. \quad (4)$$

Evaluating for  $|d\text{DM}/dt| = 2 \times 10^{-5} \text{ pc cm}^{-3} \text{ day}^{-1}$ , we find that  $R_{d\text{DM}/dt} = 3.8$  over the 150-day duration of the purported ESE. However, while the DM obtained from analyzing the entire frequency range shows a rising linear trend prior to this time period, in the split-frequency DM timeseries, the  $< 149 \text{ MHz}$  values are consistent with constant within  $\sim 1\sigma$ , and therefore there is no apparent ingress into the assumed spherically-symmetric lensing material for those frequencies. Therefore, a canonical ESE interpretation seems unlikely, though a potential DM gradient may still be plausible. Note that the egress time period occurs

<sup>1</sup> We note this measurement (and extrapolated to the estimate of the scintillation timescale discussed later) may then be useful in constraining properties in future electron density models or uncovering interesting turbulence physics along this line of sight.

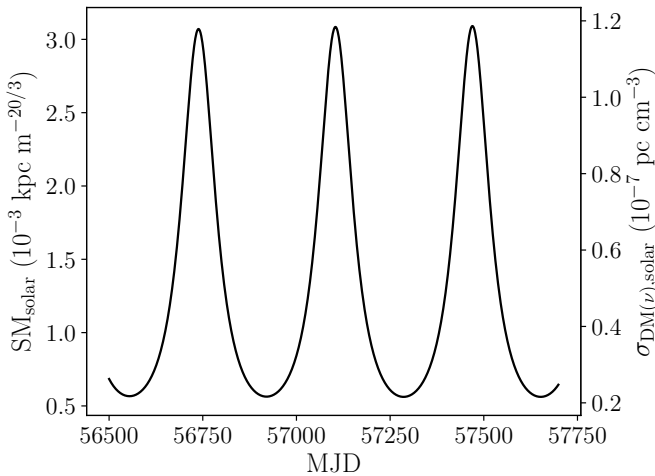


**Fig. 1.** The SM due to the solar wind along a line integrating out from the Earth to the direction of PSR J2219+4754. The right axis shows the equivalent  $\sigma_{\text{DM}(v)}$  uncertainty.

around MJD 57100, right when the DM difference between the timeseries is zero by construction. It is thus unclear if this time period truly marks the end of such an event or not.

We investigated whether this potential DM gradient could be due to the line of sight cutting through different parts of the solar wind. By MJD 56950 moving forward, the suggested time of a peak, the solar elongation is shrinking (for reference, the pulsar’s ecliptic latitude is  $52.5^\circ$ ). Thus, as the pulsar as seen on the sky approaches the Sun we would expect the DM to increase (only slightly due to the high ecliptic latitude) rather than decrease (You et al. 2007; Jones et al. 2017; Madison et al. 2018). Any solar flare or coronal events that may have occurred during this timespan would also cause an increase rather than a decrease in the DM (Lam et al. 2016b). In addition, we looked at the  $C_n^2$  contribution due to turbulence in the solar wind using the form provided in Spangler et al. (2002),

$$C_n^2(r) = 1.8 \times 10^{10} \left( \frac{r}{10 R_\odot} \right)^{-3.66} \text{ m}^{-20/3}, \quad (5)$$

where  $r$  is the radial distance from the Sun. We integrated the solar wind  $C_n^2$  over the line of sight to determine the SM, shown in Figure 1. With each integration element acting as a thin screen, we determined the frequency-dependent DM error and then combined these to find a total error of

$$\sigma_{\text{DM}(v),\text{solar}} = \sqrt{\frac{1}{\langle 1/\sigma_{\text{DM}(v)}^2(s) \rangle}}, \quad (6)$$

i.e., the total error is the square root of the reciprocal of the mean of the “weights” ( $1/\sigma^2$ ), and we are integrating along the line-of-sight position  $s$  for each volume element. We find that while the SM is increasing over the time of the suggested ESE and is of a similar value to the rest of the ISM (fiducial value of  $10^{-3.5}$ , Rickett 1977, Cordes & Rickett 1998)—because the material is very close to the Earth in comparison with the pulsar’s distance—the rms frequency-dependent DM is small, well below the measurement uncertainties and even below that of other high-precision timing experiments (see e.g., Jones et al. 2017).

For variations in DM due to the changing ionosphere, in this case because of the yearly modulation from observing the pulsar transitioning between day and night over that time period,

the amplitude of the change in DM is at most  $\sim 10^{-4}$  pc cm $^{-3}$  and therefore is not a significant contributor to the variation here (Lam et al. 2016b).

### 3.1. Impact of Non-Dispersive Delays

As has been described in the literature, there are multiple frequency-dependent delays that affect pulsar TOAs (Foster & Cordes 1990; Lam et al. 2016b, 2018b; Shannon & Cordes 2017). Beyond the traditional dispersive delay due to the integrated electron density ( $\propto \nu^{-2}$ ), there is a geometric delay ( $\propto \nu^{-4}$ ) due to total path length changes and a barycentric-correction delay ( $\propto \nu^{-2}$ ) due to the angle of arrival of the pulsar shifting, i.e., the pulsar’s image appearing from a different direction on the sky.

Following the notation in Lam et al. (2018b), the dispersive delay for a lens of size  $L$ , electron density  $n_e$ , and dispersion measure  $\text{DM}_l \sim n_e L$ , is

$$t_{\text{DM}} \sim \frac{\lambda^2 r_e \text{DM}_l}{2\pi c} \sim \frac{\lambda^2 r_e n_e L}{2\pi c}, \quad (7)$$

where  $\lambda$  is the electromagnetic wavelength,  $r_e$  is the classical electron radius, and  $c$  is the speed of light. The geometric delay is

$$t_{\text{geo}} \sim \frac{D_l(1 - D_l/D_p)\lambda^4 r_e^2 (\text{DM}'_l)^2}{8\pi^2 c} \sim \frac{D_l(1 - D_l/D_p)\lambda^4 r_e^2 n_e^2}{8\pi^2 c \zeta^2}, \quad (8)$$

where  $D_l$  and  $D_p$  are the distance to the lens and pulsar (from the observer), respectively, and  $\text{DM}'_l \sim n_e L/(\zeta L) \sim n_e/\zeta$  is the DM spatial gradient with the depth-to-length aspect ratio of the lens as  $\zeta$ . Finally, the barycentric delay is

$$t_{\text{bary}} \sim \frac{(1 - D_l/D_p)\lambda^2 r_\oplus r_e \text{DM}'_l}{2\pi c} \sim \frac{(1 - D_l/D_p)\lambda^2 r_\oplus r_e n_e}{2\pi c \zeta}, \quad (9)$$

where  $r_\oplus$  is the Earth-Sun distance of 1 AU.

Following DVT+, we assume that the cloud is spherical and therefore we set  $\zeta = 1$ . The time for the cloud to pass through the line of sight is  $\sim 300$  days. With a proper motion of 22.2 mas/yr (Michilli et al. 2018), the angle subtended on the sky is  $\theta = 18.2$  mas. The angle sets the physical size of the cloud as  $L = \theta D_l$ . Therefore, the distance of the lens is linearly proportional to the size of the lens, which is shown by DVT+ in the bottom panel of their Figure 7. Given that the DM change from the cloud is simply  $n_e L$ , we have that  $n_e$  is inversely proportional to the cloud size and inversely proportional to the lens distance, which is shown by DVT+ in the top panel of their Figure 7.

The distance estimate for a possible structure in the ISM causing light “echoes” seen in the pulse profiles is  $D_l \approx 1.1$  kpc (Michilli et al. 2018, hereafter MHD+), a companion paper to the work of DVT+. Using the DM change of  $|\delta\text{DM}| \approx 3 \times 10^{-3}$  pc cm $^{-3}$ , Figure 2 shows the dispersive, geometric, and barycentric delays for such a lensing structure at 1.1 kpc. We see that the dispersive delay dominates over the geometric and barycentric delay. However, when fitting the total frequency-dependent delays observed, the estimated infinite-frequency arrival time is shifted from the true arrival time by  $93 \mu\text{s}$ ; the estimated DM would then be larger than  $|\delta\text{DM}|$  above by  $7.1 \times 10^{-3}$  pc cm $^{-3}$ , which is unseen in the timeseries unless the baseline DM value is far lower than suggested by DVT+.

In Figure 3, we show the perturbation in  $t_\infty$  and DM (the difference between the “true” DM from the dispersive delay and that from the misestimation) after fitting the total delay curve

generated by placing a lens at a distance  $D_l$ ; again, Figure 2 shows the three frequency-dependent delays along with the total delays when  $D_l = 1.1$  kpc. These perturbations were calculated after fitting each delay curve with the functional form  $t_\nu = t_\infty + KDM/\nu^2$ . For reference, the form of these perturbations for two spot frequencies are shown in the Appendix.

If we split the total band into two halves to measure the frequency-dependence of DM, the increases in  $\delta DM$  are then  $7.3$  and  $6.8 \times 10^{-3}$  pc cm $^{-3}$  for the low and high bands, respectively, or a difference of  $5 \times 10^{-4}$  pc cm $^{-3}$  between the two. This value is approximately half of the difference between the two bands shown by DVT+ in their Figure 5. Recall, however, that in this calculation we started with a single DM, and only when estimating the DM in both halves of the band did we recover frequency dependence, solely from the unaccounted for  $\propto \nu^{-4}$  geometric delay rather than from a true DM difference. This demonstrates why a complete analysis of the arrival times, such as in Lam et al. (2018b), is crucial to understanding any potential lens/ESEs in the data rather than analyzing only the DM timeseries.

DVT+ do not show the residuals from their fit, therefore we looked at the long-term residuals in MHD+ (their Figure 1) for PSR J2219+4754 from observations covering 1970 to 2016. Figure 3 shows that the TOA perturbations due to a lens should be of order microseconds or greater depending on the distance, and for a lens at distance 1.1 kpc, we expect a perturbation of  $\approx 0.1$  ms if  $\propto \nu^{-4}$  delays are not fit for. While the residuals curve in MHD+ appears smooth, this amplitude is too small to see from the plot. MHD+ also show the evolution of the pulsar’s spindown rate. While this curve is also smoothly varying, we see a drop right at the start of 2015 (around MJD 57000), during the time of the proposed ESE. DVT+ indicate that a single spin-period derivative (MHD+ show the equivalent spin-frequency derivative) was fit in their own timing model. The spindown rate shown in MHD+ was not constant over this time period, suggesting that if the spin-frequency derivative was smaller than the average value in the fit by DVT+, then the pulsar’s spin was braking more rapidly (i.e. the spin frequency was dropping more rapidly) than expected and the infinite-frequency arrival times should be delayed compared to their model (a linear change would have been absorbed by the shorter-duration fit but we do not see that either). Any fit for DM would therefore be biased by this effect. Visualized in terms of the delay curves in Figure 2, the true arrival time would be delayed, i.e., shifted to the right.

Given the arguments above, if there was an intervening lens with a true column density equal to  $DM \approx 3 \times 10^{-3}$  pc cm $^{-3}$  that passed the line of sight, the differences in DM between the two bands could potentially be explained, but not the amplitude change of  $\approx 7 \times 10^{-3}$  pc cm $^{-3}$  in the DM timeseries from the zero value. It is possible that if a lens with a lower column density were to pass by the line of sight, it would show up with an apparent DM having the appropriate amplitude as estimated by the total time delays. One can search over the phase space of the true column density/DM, size  $L$ , and distance  $D_l$  to find the best-fit parameters of a possible lens. As stated previously, for a spherically symmetric lens, we would expect the DM timeseries from both bands to behave symmetrically.

In addition to the three delays described above, general scattering (alternatively, pulse broadening) from a Kolmogorov medium will produce arrival-time delays  $\propto \nu^{-4.4}$ . DVT+ state that if the frequency-dependent DM is variable in time, then non- $\nu^{-2}$  dispersive delays will vary equally in time. From Cordes et al. (2016), we see that the time- and frequency-dependence of DM arises naturally from ray-path averaging over different volumes of the ISM if there is an effective velocity between the

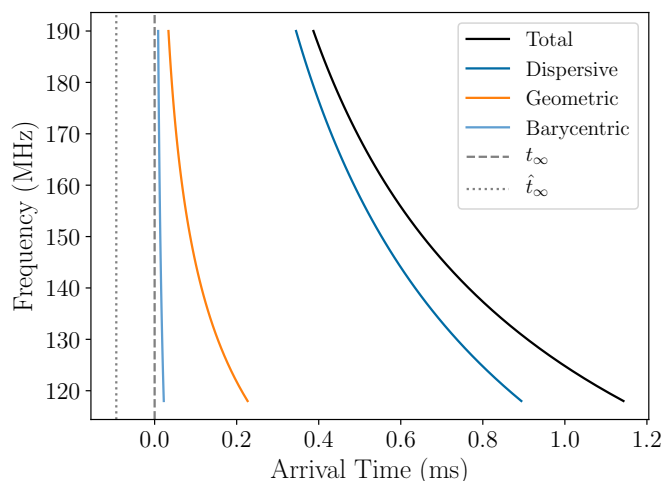


**Fig. 2.** Pulse delays as a function of time and frequency. The total delay is the sum of the dispersive, geometric, and barycentric delays. The dashed gray line shows the true infinite-frequency arrival time (set to zero) while the dotted gray line shows the estimated infinite-frequency arrival time when a purely dispersive delay is fit over all frequencies to the total delay (i.e., extrapolating the delay curve to infinite frequency),  $\delta t_\infty = -93 \mu\text{s}$ . We assume a cloud 1.1 kpc away from the Earth, the estimate for the distance in MHD+, which implies a size  $L = 20$  AU and central density  $n_e = 31 \text{ cm}^{-3}$  (from our analysis but also see Figure 7 of DVT+). For clarity, the legend from top to bottom displays the different curves from right to left.

Earth, pulsar, and bulk ISM motions. (Regarding the effective velocity, see Cordes & Rickett 1998). Such variations can arise even for a medium with constant  $C_n^2$ , which for example can yield a statistically constant scattering timescale even while the DM varies. Changes in the scattering timescales have been observed (e.g., Coles et al. 2015; Levin et al. 2016), which require a change in  $C_n^2$  (or the inner scale of the turbulence, again see Cordes & Rickett 1998) and therefore the *statistics* of the DM variations, though the timeseries of each need not be one-to-one correlated. As with the geometric and barycentric delay, a  $\propto \nu^{-4.4}$  scattering delay will also cause DM to be incorrectly estimated if not properly modeled.

### 3.2. Impact of Frequency- and Time-Dependent Profile Evolution

The variability of the pulse profile of PSR J2219+4754 with time was discussed in MHD+ in the context of light echoes due to propagation effects. Bilous et al. (2016) showed in an observation taken in early 2014 (around MJD 56700) that there was significant frequency dependence in the pulse profile. Using profiles of PSR J2219+4754 from Bilous et al. (2016)<sup>2</sup>, we examined the TOA and DM perturbations due to the frequency dependence of the profiles. These four profiles are shown in Figure 4; the trailing components are clearer at lower frequencies than at higher frequencies, suggesting that the shape variations as a function of time as seen in MHD+ are also a function of frequency, at least for some epochs.

Bilous et al. (2016) used their observations to determine a new spin period and DM for each of the pulsars in their census. The initial adjustment of these two parameters maximized the

<sup>2</sup> Obtained via the European Pulsar Network, <http://www.jb.man.ac.uk/research/pulsar/Resources/epn/>

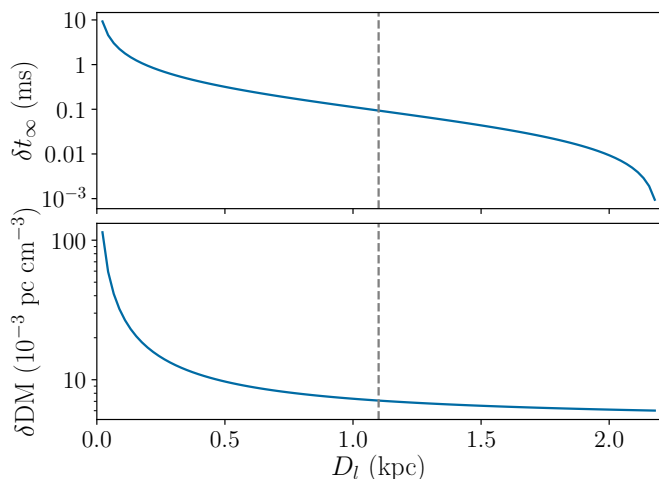


**Fig. 3.** The TOA perturbation and DM perturbation when fitting for the set of total frequency-dependent delays (e.g., see Figure 2) versus only the dispersive delay. We display these perturbations as a function of the lens distance.

pulse signal-to-noise ratio. Afterward, an average template was generated, which was used to calculate more precise TOAs and perform a subsequent timing analysis to improve their period and DM estimate. They did not account for profile evolution, either intrinsic or from interstellar scattering, in their work but noted it as a potential bias; the profiles used in this analysis are therefore phase-aligned according to their method.

We generated smooth template shapes for each of the four profiles. While pulsar components are often fit with von Mises functions (e.g., Osłowski et al. 2011; Hassall et al. 2012), the circular analogue of a Gaussian function, the automated routine in the `PyPULSE` package (Lam 2017) to fit multiple such components (see a more thorough description of the procedure conditions in Lam et al. 2019) did not converge for the lower-frequency profiles due to the shapes of the trailing components. We then used a simpler Savitzky-Golay filter (Savitzky & Golay 1964), implemented in `scipy` with a moving 11-point cubic polynomial, which produced residuals between the template and the data profile at the level of the rms noise of the off pulse region; slight variations in the parameters did not affect the overall fit significantly. With our four smooth pulse shapes, we used `PyPULSE` to fit the highest-frequency (178 MHz) template to the other three templates in order to compute the arrival-time offsets due to frequency-dependent profile evolution; these were 229.0, 75.7, and 11.2  $\mu\text{s}$  for the 120, 139, and 159 MHz profiles, respectively. We chose the highest-frequency template as a standard of comparison to minimize the impact of the trailing component shapes as an approximation for the intrinsic pulse shape compared to a pulse shape showing a light echo.

Using these timing perturbations, we then calculated the estimated DM perturbations; see the Appendix for more on DM estimation in the presence of an additional chromatic perturbation, in this case delays due to the pulse shape changes as a function of frequency. Since the method of calculating DM between Bilous et al. (2016) and this analysis are different, we do not expect the absolute DM value to be the same (Lam et al. 2016b). However, using the two lowest or highest frequencies to calculate the DM alone yielded a difference between the two of  $1.7 \times 10^{-3} \text{ pc cm}^{-3}$ , again of the same amplitude of the variations seen by DVT+. This value is an order of magnitude larger than the DM differ-

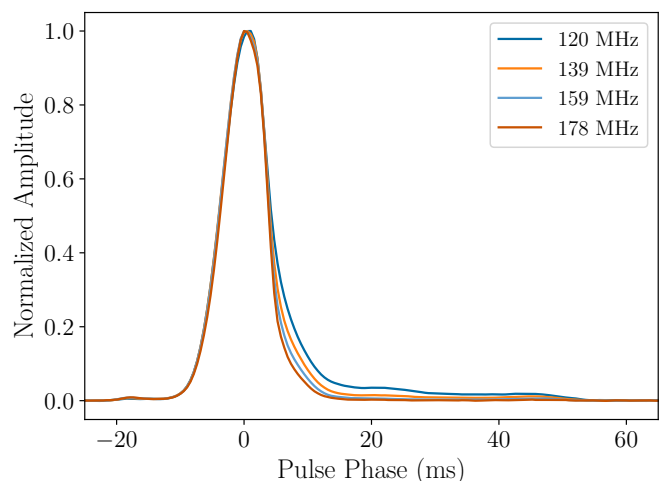


**Fig. 4.** Profiles of PSR J2219+4754 as a function of frequency from Bilous et al. (2016). The pulse phase is centered at the peak and only a small part around the main pulse is shown for clarity.

ence quoted between scattered and unscattered profiles, though it is unclear which profiles they refer to. In performing their DM analysis, DVT+ accounted for frequency-dependent profile evolution with a frequency-resolved template, which should then mitigate any impact of this profile evolution on the measured DMs. As mentioned previously, since their template was generated from an observation on MJD 57161, we expect the DM at both bands to be equal by construction at that epoch, which is also noted by the authors, though the true absolute DM between the two at that time and over the course of the entire observing span may differ. Nevertheless, the changing profile shapes as a function of time as seen in DVT+ and in MHD+ could cause biases in the TOAs and the subsequent DM determinations, especially when coupled with the changes in frequency.

### 3.3. Impact of Arrival-Time Uncertainties

We examined the role of additional errors to the TOA uncertainties due to pulse jitter on the DM estimates. Traditionally until the last several years, many analyses considered the TOA uncertainty as arising only from template fitting (e.g., Manchester et al. 2013; Demorest et al. 2013; Desvignes et al. 2016), the process of fitting a smoothed template shape to the data profile. The assumption of matched filtering which underlies this fitting is that the data is a shifted and scaled copy of the template shape. It has been long known that single pulses from pulsars vary stochastically (Craft 1970), implying that the data shape cannot be an exact copy of a template since the average of a finite number of single pulses will always be slightly different. In general, shape changes due to jitter include contributions both from phase and amplitude variations.

We use the jitter parameter  $f_j$  defined in Cordes & Downs (1985) for our analysis, defined as the ratio between the single-pulse rms jitter and the equivalent rms (i.e., for a Gaussian pulse, the standard deviation as compared to the full width at half maximum) of the template (Shannon et al. 2014; Lam et al. 2016a). Cordes & Shannon (2010) summarize a number of analyses in the literature, primarily for canonical pulsars, and suggest that  $f_j \approx 1/3 - 1/2$ . Shannon et al. (2014) find similar values for millisecond pulsars. Lam et al. (2016a, 2019) use a separate jitter parameter that is independent of the pulse shape but find compa-

rable statistics for millisecond pulsars. In many cases, especially for bright canonical pulsars in which single pulses can be detected, jitter is the dominant component of the TOA uncertainty (Lam et al. 2016a).

Again using profiles of PSR J2219+4754 from Bilous et al. (2016), calculating the pulse width, and assuming a fiducial value of  $f_j = 1/3$ , we found the rms single-pulse jitter for PSR J2219+4754 to be 1.2 ms,  $\approx 0.2\%$  of pulse phase ( $P = 0.5385$  s), consistent with some pulsars in Lam et al. (2016a, 2019) though below the average. (Note that millisecond pulsar studies as described above were performed at significantly higher frequencies, and the statistics for millisecond pulsars may be different from that of canonical pulsars.) Since the rms jitter scales as the number of pulses  $N_p^{-1/2}$ , we assumed the pulsar was observed for the median observing time each epoch, 115 minutes, using the LOFAR station most used in DVT+, DE605. Given the number of pulses in that time, we find that the TOA uncertainty due to jitter is  $\approx 10 \mu\text{s}$ . Using a larger value of the jitter parameter(s) will yield a larger uncertainty. In addition, changes in the integration time will vary the TOA uncertainty; the integration times for DE605 ranged from 2 to 146 minutes, which yield an equivalent rms jitter of  $79 \mu\text{s}$  to  $9 \mu\text{s}$ , respectively.

DVT+ do not show timing residuals or provide the statistics of their arrival time uncertainties, but do note that they use the formal uncertainties from template fitting (Taylor 1992) in their TOA analysis. We estimate the value of these uncertainties as follows. DVT+ state a median DM uncertainty of  $3.7 \times 10^{-5} \text{ pc cm}^{-3}$ . Following the formalism of Lam et al. (2015) and Cordes et al. (2016) of assuming that the (frequency-independent) DM is measured at two spot frequencies and then the infinite-frequency TOA is estimated by removing the dispersive delay, one can calculate the DM difference between the true DM and the estimated DM as

$$\delta\text{DM} = -\frac{\epsilon_{\nu_1} - \epsilon_{\nu_2}}{K(\nu_1^{-2} - \nu_2^{-2})}, \quad (10)$$

where  $K \approx 4.149 \times 10^9 \mu\text{s MHz}^2 \text{ pc}^{-1} \text{ cm}^3$  is the dispersion constant Lorimer & Kramer (2012) and  $\sigma_{\epsilon_\nu}$  is the rms timing uncertainty for frequency  $\nu$ . (See the Appendix for more on this derivation and its effect on TOA perturbation.) The rms DM uncertainty,  $\sigma_{\delta\text{DM}}$ , is then  $\langle(\delta\text{DM})^2\rangle^{1/2}$ . Assuming that  $\sigma_{\epsilon_\nu}$  is the same for the two halves of the LOFAR band and that  $\sigma_{\delta\text{DM}} = 3.7 \times 10^{-5} \text{ pc cm}^{-3}$ , we find that  $\sigma_{\epsilon_\nu} \approx 2.3 \mu\text{s}$ . This is a factor of four smaller than the jitter uncertainty described above and does further suggest that the only uncertainties considered are from the finite signal-to-noise ratio rather than including jitter (otherwise the value of  $\sigma_{\epsilon_\nu}$  we found would be larger). This TOA uncertainty may also include any unmitigated frequency-dependent scatter in the arrival times, e.g., from non- $\nu^{-2}$  delays, and so it is possible that the true template-fitting uncertainties are in fact smaller.

If the total TOA uncertainty is then the square root of the quadrature sum of the previous TOA uncertainty of  $2.3 \mu\text{s}$  and the rms jitter of  $10 \mu\text{s}$ , we can solve for the corrected rms DM uncertainty and find that  $\sigma_{\delta\text{DM}} = 1.7 \times 10^{-4} \text{ pc cm}^{-3}$ . This is the rms DM uncertainty determined over the whole frequency band. Next we calculate new DM uncertainties assuming that DM is derived from each half of the band separately (making sure to correct the TOA uncertainties for the change in the signal-to-noise ratio by a factor of  $\sqrt{2}$  but no change in the jitter as it is roughly frequency-independent over a small frequency range; Lam et al. 2019), as is done by DVT+ to find the DM using measurements taken above and below 149 MHz. We have split

the full band into four and then used the centers of the bottom two frequency channels as our spot frequencies to determine the DM for data taken below 149 MHz. Correspondingly the centers of the top two frequency channels were used to determine the DM for data taken above 149 MHz. We find that  $\sigma_{\delta\text{DM}} = 3 - 5 \times 10^{-4} \text{ pc cm}^{-3}$ . This range of values is of similar order to those of  $\sigma_{\text{DM}(\nu)}$  discussed in §2. Our analysis describing the underestimation of the TOA uncertainties further strengthens the argument that differences in DM between the two frequency bands discussed in DVT+ are less significant than are shown. We do note, however, that while the amplitude of these uncertainties adds significantly to the two DM timeseries, this is a white-noise contribution in time and, therefore, cannot explain the systematic offsets between the two that are seen by DVT+.

We also estimated the contribution to the TOA uncertainty from scintillation noise, also known as the ‘‘finite-scintle effect’’ (Cordes et al. 1990), one of three commonly-analyzed white-noise contributions to the TOA uncertainty on short timescales (Lam et al. 2016a, 2018a). The scintillation timescale  $\Delta t_d$  can be found when the structure function of the electromagnetic phase perturbation is equal to 1, or alternatively in terms of the DM structure function (Lam et al. 2016b),

$$D_{\text{DM}}(\Delta t_d) = 1.47 \times 10^{-15} (\text{pc cm}^{-3})^2 \left(\frac{\nu}{\text{GHz}}\right)^2. \quad (11)$$

Given that they observe  $D_{\text{DM}}(\tau) = 3.1 \times 10^{-10} (\text{pc cm}^{-3})^2 (\tau/\text{day})^{5/3}$ , we find that  $\Delta t_d = 5.7$  s. Due to the time-variability of the trailing components in the profile, we estimate the scattering timescale simply from NE2001 as  $\tau_d = 0.4$  ms at 150 MHz, or an equivalent scintillation bandwidth of  $\Delta \nu_d = 0.46$  kHz. The TOA uncertainty from scintillation noise is  $\approx \tau_d / \sqrt{n_{\text{ISS}}}$ , where  $n_{\text{ISS}}$  is the number of scintles (‘‘patches’’ of increased intensity in the time-frequency plane), given by

$$n_{\text{ISS}} \approx \left(1 + \eta_t \frac{T}{\Delta t_d}\right) \left(1 + \eta_\nu \frac{B}{\Delta \nu_d}\right). \quad (12)$$

The filling factors  $\eta_t, \eta_\nu$  are in the range 0.1-0.3 depending on the properties of the medium, and we have adopted a value of 0.2 for both (Cordes & Shannon 2010). Given an observation time  $T = 115$  minutes and a bandwidth  $B = 71.5$  MHz, we find that contribution of scintillation noise to the TOA uncertainty is  $0.4 \mu\text{s}$ , much smaller than either the template-fitting component or the jitter component, and therefore it should not factor into the error budget substantially.

Lastly, we looked at the impact of polarization calibration errors on the data (Stinebring et al. 1984). Foster et al. (2015) have shown that polarization leakage can result in significant TOA uncertainties ( $\sim$ microseconds) for well-timed millisecond pulsars. Gentile et al. (2018) showed that the stability of the Arecibo Observatory system varies quite dramatically between frequencies and epochs and therefore re-calibration must be performed per epoch. Given the errors, we believe it important to examine the calibration procedure of DVT+, who follow Noutsos et al. (2015), where PSR J2219+4754 itself was used to test the calibration stability of the LOFAR antennas. Noutsos et al. (2015) state that systematic uncertainties in the polarization leakage are of order 5–10%.

DVT+ performed observations at or close to transit, and therefore claim that imperfections in the calibration did not affect the analysis. However, Noutsos et al. (2015) show that at hour angles far away from transit, the profile differences for PSR J2219+4754 can be as large as 30% compared with at

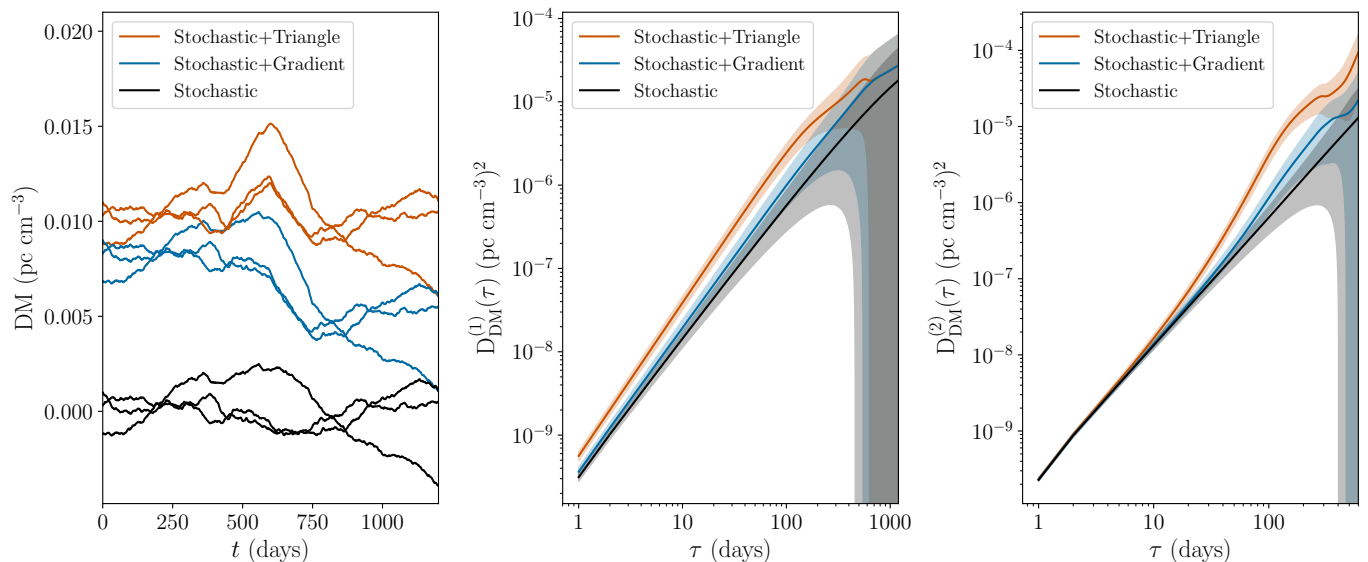


**Fig. 5.** DM timeseries (left) along with their associated first- (middle) and second-order (right) structure functions. We plot the first three (arbitrary) timeseries we generated of the stochastic DM component (black) and added in a gradient (blue) or a triangle function representing an ESE (red). We offset the timeseries by  $+0.005 \text{ pc cm}^{-3}$  between each set of three for visual clarity. The corresponding structure functions have the same colors, where the lines and the shaded regions represent the mean and standard deviation, respectively. See the text for more information.

transit for the circularly polarized flux. While the observations DVT+ performed were closer to transit, we would still expect pulse shape deviations of order a few percent given the observation lengths alone.

Following Cordes et al. (2004), the TOA uncertainty due to pulse shape changes from an incorrect absolute gain calibration is

$$\sigma_{\text{pol}} \sim 1 \mu\text{s} \left( \frac{\varepsilon}{0.1} \right) \left( \frac{\pi_V}{0.1} \right) \left( \frac{W}{100 \mu\text{s}} \right), \quad (13)$$

where we provide fiducial values as in Lam et al. (2016a, 2018a) for the fractional gain error  $\varepsilon$ , degree of circular polarization  $\pi_V$ , and pulse width  $W$ . Using Eq. 13 as a crude estimator, with a pulse with of  $\sim 8 \text{ ms}$ , a circular polarization fraction of 9% (Noutsos et al. 2015), and assuming  $\varepsilon \sim 0.1$  (the gain error and polarization leakage are not entirely equivalent quantities but we take the fractional errors above as representative), then the component of the TOA uncertainty is  $\sim 72 \mu\text{s}$ , many times larger than the template-fitting errors. If polarization error yields a consistent offset/perturbation in the arrival times, then the net stochastic TOA uncertainty is zero and the frequency-dependent DM analysis should not be affected. However, given analyses such as that of Gentile et al. (2018) regard system stability, we do not expect these calibration errors to be systematic alone. While PSR J2219+4754 is not a millisecond pulsar, we see that it is quite likely that polarization calibration errors on the order of microseconds or tens of microseconds are expected (see again Foster et al. 2015), which since comparable to the template-fitting errors, should further be accounted for in dispersive-delay removal.

### 3.4. Impact of a DM Gradient on the Structure Function

Any additional structure in the DM timeseries beyond that from a turbulent medium will increase the measured structure function (Lam et al. 2016b; Jones et al. 2017). For the following analysis, we will make a distinction between the first-order structure func-

tion  $D_{\text{DM}}^{(1)}(\tau)$  that we have implicitly discussed previously and the second-order structure function  $D_{\text{DM}}^{(2)}(\tau)$ , both defined as follows:

$$\begin{aligned} D_{\text{DM}}^{(1)}(\tau) &\equiv \langle [\text{DM}(t + \tau) - \text{DM}(t)]^2 \rangle, \\ D_{\text{DM}}^{(2)}(\tau) &\equiv \langle [\text{DM}(t + \tau) - 2\text{DM}(t) + \text{DM}(t - \tau)]^2 \rangle. \end{aligned} \quad (14)$$

While the first-order structure function will remove any constant term from the timeseries (e.g., the mean), the second-order structure function removes linear terms and can be used to detect discrete changes in any underlying linear trends in the DM timeseries (Lam et al. 2016b). The latter can also be thought of as related to the curvature of the timeseries. For a Kolmogorov medium, it is related to the first-order structure function (Lam et al. 2016b, Appendix A). Again, any additional structures beyond a turbulent medium seen in the timeseries will increase these measured quantities.

To understand the impact of a DM gradient or ESE on the structure functions of both orders, we performed simulations as in Lam et al. (2015, 2016b) of red-noise realizations of DM timeseries. We generated 10,000 realizations of 1200-day DM timeseries from a stochastic Kolmogorov medium for which the amplitude was set by the measured structure function  $D_{\text{DM}}(\tau) = 3.1 \times 10^{-10} (\text{pc cm}^{-3})^2 (\tau/\text{day})^{5/3}$ . Next, we added a gradient with slope  $2 \times 10^{-5} \text{ pc cm}^{-3} \text{ day}^{-1}$  and of length 150 days into each timeseries. To avoid a discontinuity, we added a baseline value of  $3 \times 10^{-3} \text{ pc cm}^{-3}$  to the higher side of the gradient (i.e., in total we added a slanted step function). Lastly, we added a triangle function representing an ESE into each stochastic realization (separate from the gradient), with slope  $2 \times 10^{-3} \text{ pc cm}^{-3} \text{ day}^{-1}$  and of length 150 days on either side. Figure 5 (left panel) shows several of these timeseries.

As expected, we see in the first-order structure functions shown in the middle panel that there is an increase in the amplitude as well as a changing slope, though the mean stochastic + gradient structure function is within one standard deviation of the mean stochastic-only structure function. Note that because the length of the actual timeseries is only 1200 days, the

range of  $D_{\text{DM}}^{(1)}$  at large lag varies significantly from the mean at lags greater than a few hundred days, differing from Figure 6 of DVT+, which we were able to reproduce when taking the standard deviation of the (base-10) logarithm of the structure function. Since only a few increments (DM differences) contribute to the averages in the bins at large lags, we do expect a wide variation as we see in Figure 5 and in previous simulations of ours (Lam et al. 2015, 2016b).

If either a density gradient or an ESE is along the line of sight, then the stochastic Kolmogorov component of the measured first-order structure function should be lower in amplitude than previously reported, thereby lowering the measured SM or raising the scintillation timescale. While the slope of the mean first-order structure function for the stochastic + triangle simulations has a steeper slope, the “realization errors” on the structure function for the stochastic-only simulations can lead to both steeper or shallower slopes for a single measured structure function, which must be accounted for when performing these analyses to constrain the consistency of the spectrum with a Kolmogorov medium without bias (Lam et al. 2016b; Jones et al. 2017).

DVT+ did not perform an analysis of the second-order DM structure function (such an analysis is uncommon in the literature for DM timeseries); we show the results of our analysis in the right panel of Fig 5. We notice two features. First, all three structure functions tend toward the same value at low time lags, which may then allow for a more robust estimate of the scintillation timescale (or alternatively the SM as in DVT+) as per Appendix A of Lam et al. (2016b). Second, we see that adding extra components to the DM timeseries on top of the purely stochastic term will produce a more pronounced increase in the value of the second-order structure function at a time lag of  $\sim 150$  days, the timescale of the injected structures. There is still some slight overlap in the mean stochastic + gradient versus the mean stochastic-only second-order structure function. Due to irregular sampling in DM timeseries, common for many pulsar observations, it may be preferred to analyze the individual second-order increments ( $\text{DM}(t+\tau) - 2\text{DM}(t) + \text{DM}(t-\tau)$ ), which are squared and averaged over to obtain  $D_{\text{DM}}^{(2)}$  as was performed for PSR B1534+12 in Lam et al. (2016b) than the second-order structure function as performed here.

Note that the large transverse velocity means that the motion of the pulsar across the sky is fairly straight (e.g., the parallax motion is small, see trajectory plots in Jones et al. 2017). The quasi-periodic variations in the DM timeseries that deviate from a purely power-law spectrum, seen in Madison et al. (2018) due to the line of sight crossing correlated spatial DM fluctuations, should therefore be small and not impact the power spectrum/structure function significantly. Put another way, while the assumption of the line of sight crossing independent DM fluctuations is broken and we expect short-term rapid variations in the DM that might impact the measured structure function, we expect this change to be negligible for this pulsar.

#### 4. Impact on Precision Timing

DVT+ discuss the effects of DM variations on high-precision pulsar timing and its applications, including the efforts to detect low-frequency gravitational waves. The authors first state that the long-term trends in DM will be of limited impact on these timing experiments given our ability to correct for them. They next describe the problematic impact of correcting for DM in high-frequency observations in those observations alone. Lastly,

they express concern in including low-frequency data for measurements of DM variations.

While we agree with these points, in principle, we have several concerns with these conclusions. First, the authors estimate the limiting TOA precision by considering observations at 1.4 GHz with a relatively limited 250 MHz bandwidth (20% bandwidth). By contrast, current pulsar backend systems can process up to 800 MHz of bandwidth (e.g., Arzoumanian et al. 2018, though the usable bandwidth is closer to 600-650 MHz, see Arzoumanian et al. 2015) and techniques have been developed to process even larger bandwidths (e.g., Dunning et al. 2015) while simultaneously compensating for the DM (Pennucci et al. 2014). More generally, a common practice is to conduct simultaneous or near-simultaneous observations at two frequencies (e.g., the North American Nanohertz Observatory for Gravitational Waves, NANOGrav, uses combinations of 0.8 GHz and 1.4 GHz for some pulsars and 1.4 GHz to 2.3 GHz for some others), from which even higher precision DM estimates can be obtained.

When only purely dispersive delays factor into TOAs measured at two spot frequencies, the rms TOA is given by (see the Appendix but also Lee et al. 2014, Eqn. 12; Lam et al. 2018a, Table 1),

$$\sigma_{\delta t_{\infty}} = \left( \frac{\sigma_{\epsilon_{\nu_1}}^2 + r^4 \sigma_{\epsilon_{\nu_2}}^2}{(r^2 - 1)^2} \right)^{1/2}, \quad (15)$$

where again  $\sigma_{\epsilon_{\nu}}$  is the rms timing uncertainty for frequency  $\nu$ . This timing uncertainty includes all sources of white noise that affect the TOA estimation, such as from radiometer noise or jitter (see e.g., Lam et al. 2018a). A critical aspect of Eq. 15 is that the rms TOA is dependent only on  $r$  and not a specific frequency. It does not matter whether the timing measurements are acquired at low or high frequencies so long as the individual frequency-channel TOA uncertainties are the same for a given value of  $r$ .

As an illustration, taking  $r \sim 2$  and setting  $\sigma_{\epsilon_{\nu_2}} = \sigma_{\epsilon_{\nu_1}} = \sigma_{\epsilon_{\nu_2}}$ , then  $\sigma_{\delta t_{\infty}} = 1.4\sigma_{\epsilon_{\nu_1}}$ . Therefore, in cases where the median TOA uncertainty from finite pulse signal-to-noise ratio is small (i.e., well below 1  $\mu\text{s}$ ), such as reported per-pulsar and per-band in the NANOGrav 11-Year Data Set (Arzoumanian et al. 2018), then the requirement for sub-microsecond precision timing is met. Several other sources of error, such as from pulse phase jitter, are known to be much smaller than this limit (Lam et al. 2019). Therefore, using low-frequency timing data to increase  $r$  will quantitatively improve the timing of many pulsars as long as the TOA uncertainties for pulses at those frequencies are low enough and unmitigated ISM effects are small, e.g., typically for pulsars with lower DM values (Lam et al. 2018a).

As an extreme case, we consider  $\sigma_{\epsilon_{\nu_2}} \rightarrow 0$ . In this case, the overall timing precision will be dominated by the precision at the lower frequency,  $\sigma_{\delta t_{\infty}} \approx \sigma_{\epsilon_{\nu_1}} / (r^2 - 1)$ . For a sufficiently large value of  $r$ , the timing precision due to DM uncertainty or variations could be made negligible. As a specific example, with relevance to the data presented by DVT+, we consider  $r \approx 10$ , equivalent to  $\nu_1 \approx 140$  MHz and  $\nu_2 \approx 1400$  MHz. In this hypothetical example, a timing precision  $\sigma_{\delta t_{\infty}} \approx 10$  ns could be obtained, if  $\sigma_{\epsilon_{\nu_1}} \approx 1 \mu\text{s}$ . We have chosen this illustration because a timing precision of order 10 ns is comparable to the expected precision required for the study of gravitational waves.

This timing improvement of course neglects the uncertainties due to frequency-dependent DM as discussed by Cordes et al. (2016). The amplitude of the differences in DM between frequencies also depends on  $r$  (as well as the specific frequency choices) but the net effect on the overall timing precision can



be quantified and then built into noise models, e.g., via covariance matrices such as constructed in Lam et al. (2018a). Cordes et al. (2016, Figures 7 and 8) show that for pulsars with  $DM \lesssim 30 \text{ pc cm}^{-3}$ , combining data from the 100 MHz and 2 GHz regimes will yield TOA errors that still meet the requirement of sub-microsecond precision, especially as current and future telescopes come online, drastically reducing the template-fitting errors from finite pulse signal-to-noise ratio. Many pulsars used in precision-timing experiments have DM values in this range (Verbiest et al. 2016). Cordes et al. (2016) also discuss fitting a wide range of frequencies versus only two spot values; as expected, the increase in frequency coverage can in many cases improve the timing precision over the case where only two spot frequencies are used, which is no longer the case for many modern precision-pulsar-timing experiments (Verbiest et al. 2016).

Unmitigated chromatic delays will also add to the TOA uncertainties (Lam et al. 2018a, Table 1) and cause frequency-dependent excess noise in the timing residuals (Lentati et al. 2016; Lam et al. 2017). However, even for the pulsar with the highest DM millisecond pulsar used in precision timing, PSR J1903+0327 ( $DM \approx 300 \text{ pc cm}^{-3}$ ), observed between roughly 1.1 and 2.5 GHz, the long-term rms residual is  $4 \mu\text{s}$ , though a significant portion of that rms is again from frequency-dependent excess noise (Lam et al. 2017), which future timing methodologies might be able to mitigate partially (Shannon & Cordes 2017).

Lastly, we comment on the statement in DVT+ that at higher frequencies, longer-term DM variations are of particular importance to take into account for timing data. Given that the frequency-dependent DM comes from difference in ray-path averaging whereas the trends in DM come from the relative Earth-pulsar motion along the line of sight, we expect the longer-term DM variations to track each other between frequencies, regardless of frequency; DVT+ also agree with this given their analysis. However, in terms of the overall timing, it is the lower frequencies that are impacted much more heavily since the dispersive delays are weighted by  $\nu^{-2}$ . At frequencies much higher than typically used in precision timing, the dispersive delay becomes small and thus any changes in the dispersive delay are also small; as an extreme, X-ray pulsar data do not require DM corrections of any kind.

As an additional consideration, it is important to remember that short-term DM variations that are improperly corrected for can contribute heavily to the overall rms timing, and may not contribute as simple white noise (e.g., Lam et al. 2015). Many pulsars in precision-timing experiments show very rapid timescales for DM to vary (Jones et al. 2017), including from the solar wind (You et al. 2007; Madison et al. 2018; see also Howard et al. 2016 for the study of a coronal mass ejection with a slow-period pulsar) or structures in the ISM (e.g., Fonseca et al. 2014; Coles et al. 2015; Lam et al. 2018b).

## 5. Discussion

Going forward, analyses of observations of the kind reported in DVT+ must account for the wide range of different TOA uncertainty components and ISM propagation effects. We see here that even for a canonical pulsar versus a millisecond pulsar, the recent work done in precision-timing experiments has become relevant given the timing quality of the pulsars and the instrumentation used to access to new types of observations, e.g., low-frequency observations via LOFAR as described here. And while canonical pulsars may not provide constraints on the same tests of fundamental physics as millisecond pulsars, their use in studying

variations in the ionized ISM along many different lines of sight (e.g., Petroff et al. 2013) will be unparalleled given the greater population of them over millisecond pulsars, especially if observations covering a large frequency ratio can be leveraged.

Identifying ESEs or other ‘‘ISM events’’ seen in pulsar timing data in near-real time will allow for more intensive followup observations, including a higher cadence of observations over many frequencies and using different observatories worldwide, especially if dynamic spectra with resolved scintles can be obtained (Hewish 1980; Stinebring et al. 2001). Interferometric observations can help constrain the changing position and sizes of the pulsar image (Blandford & Narayan 1985), or possibly multiple images (Cordes & Wolszczan 1986; Cordes et al. 2017), and provide additional constraints on the line of sight. Any such additional observations will allow us to resolve small-scale structure in the ISM and probe the Galactic population of these lenses.

*Acknowledgements.* The NANOGrav Project receives support from NSF Physics Frontiers Center award number 1430284. Part of this research was carried out at the Jet Propulsion Laboratory, California Institute of Technology, under a contract with the National Aeronautics and Space Administration. Part of this research has made use of the database of published pulse profiles maintained by the European Pulsar Network, available at: <http://www.jb.man.ac.uk/research/pulsar/Resources/epr/>.

## Appendix A: DM Estimation with Additional Chromatic Errors

As a useful reference, here we will describe DM estimation from observations taken at two spot frequencies with additional chromatic errors following the formalism of Lam et al. (2015) and Cordes et al. (2016). We can write the TOA at a particular frequency  $\nu$  as the infinite-frequency arrival time plus the dispersive delay term. For this calculation, we will also include measurement errors  $\epsilon_\nu$  and a chromatic (frequency-dependent) timing perturbation  $t_{C,\nu}$ , such that

$$t_\nu = t_\infty + \frac{KDM}{\nu^2} + t_{C,\nu} + \epsilon_\nu. \quad (\text{A.1})$$

Here,  $K \approx 4.149 \times 10^9 \mu\text{s MHz}^2 \text{ pc}^{-1} \text{ cm}^3$  is the dispersion constant in observationally convenient units (Lorimer & Kramer 2012). We estimate the DM by taking TOAs at two frequencies  $\nu_1$  and  $\nu_2$  and calculating

$$\widehat{DM} = \frac{t_{\nu_1} - t_{\nu_2}}{K(\nu_1^{-2} - \nu_2^{-2})}. \quad (\text{A.2})$$

As in the main text, we will define the frequency ratio  $r \equiv \nu_2/\nu_1$  with  $\nu_1 < \nu_2$ . The estimated infinite-frequency arrival time can then be written in one of two ways as

$$\begin{aligned} \hat{t}_\infty &= t_{\nu_1} - \frac{K\widehat{DM}}{\nu_1^2} = t_\infty + \frac{K(DM - \widehat{DM})}{\nu_1^2} + t_{C,\nu_1} + \epsilon_{\nu_1} \\ &= t_{\nu_2} - \frac{K\widehat{DM}}{\nu_2^2} = t_\infty + \frac{K(DM - \widehat{DM})}{\nu_2^2} + t_{C,\nu_2} + \epsilon_{\nu_2} \end{aligned} \quad (\text{A.3})$$

We will now solve for the DM difference. Substituting the measured TOAs  $t_\nu$  into the equation for  $\widehat{DM}$  and subtracting from the true DM, we have

$$\begin{aligned} \delta DM \equiv DM - \widehat{DM} &= DM - \frac{t_{\nu_1} - t_{\nu_2}}{K(\nu_1^{-2} - \nu_2^{-2})} \\ &= -\frac{t_{C,\nu_1} - t_{C,\nu_2} + \epsilon_{\nu_1} - \epsilon_{\nu_2}}{K(\nu_1^{-2} - \nu_2^{-2})}. \end{aligned} \quad (\text{A.4})$$

The TOA perturbation will be

$$\begin{aligned}\delta t_\infty \equiv t_\infty - \hat{t}_\infty &= -\frac{K(\text{DM} - \widehat{\text{DM}})}{v_2^2} - t_{C,v_2} - \epsilon_{v_2} \\ &= \frac{-r^2 t_{C,v_2} - r^2 \epsilon_{v_2} + t_{C,v_1} + \epsilon_{v_1}}{r^2 - 1}.\end{aligned}\quad (\text{A.5})$$

When the chromatic offsets are zero, we arrive at simply

$$\delta t_\infty = \frac{\epsilon_{v_1} - r^2 \epsilon_{v_2}}{r^2 - 1}, \quad (\text{A.6})$$

which agrees with Eq. 21 in Cordes et al. (2016) assuming the frequency-dependent DM term is zero.

Eq. A.6 provides the timing offset but one must consider the TOA uncertainty,  $\sigma_{\delta t_\infty}$ , from the variance

$$\sigma_{\delta t_\infty}^2 = \langle \delta t_\infty^2 \rangle = \left\langle \left( \frac{\epsilon_{v_1} - r^2 \epsilon_{v_2}}{r^2 - 1} \right)^2 \right\rangle. \quad (\text{A.7})$$

We have assumed here that  $\langle \delta t_\infty \rangle = 0$ , which will be true if the errors  $\epsilon_v$  are Gaussian distributed. If they are, and with variance  $\sigma_{\epsilon_v}^2$ , then the sum of the two terms in the numerator of Eq. A.7 will be Gaussian distributed, which when squared will then be chi-squared distributed. Taking the expected value of the resultant quantity yields

$$\sigma_{\delta t_\infty}^2 = \frac{\sigma_{\epsilon_{v_1}}^2 + r^4 \sigma_{\epsilon_{v_2}}^2}{(r^2 - 1)^2}. \quad (\text{A.8})$$

If the TOA uncertainties are the same at both frequencies such that  $\sigma_{\epsilon_{v_1}} = \sigma_{\epsilon_{v_2}} = \sigma_{\epsilon_v}$ , then we have

$$\sigma_{\delta t_\infty} = \sqrt{\langle \delta t_\infty^2 \rangle} = \sigma_{\epsilon_v} \left( \frac{r^4 + 1}{r^4 - 2r^2 + 1} \right)^{1/2}. \quad (\text{A.9})$$

## References

Armstrong, J. W., Rickett, B. J., & Spangler, S. R. 1995, *ApJ*, 443, 209  
Arzoumanian, Z., Brazier, A., Burke-Spolaor, S., et al. 2015, *ApJ*, 813, 65  
Arzoumanian, Z., Brazier, A., Burke-Spolaor, S., et al. 2018, *ApJS*, 235, 37  
Backer, D. C., Hama, S., van Hook, S., & Foster, R. S. 1993, *ApJ*, 404, 636  
Bilous, A. V., Kondratiev, V. I., Kramer, M., et al. 2016, *A&A*, 591, A134  
Blandford, R., & Narayan, R. 1985, *MNRAS*, 213, 591  
Cognard, I., Bourgois, G., Lestrade, J.-F., et al. 1993, *Nature*, 366, 320  
Coles, W. A., Kerr, M., Shannon, R. M., et al. 2015, *ApJ*, 808, 113  
Cordes, J. M., & Downs, G. S. 1985, *ApJS*, 59, 343  
Cordes, J. M., & Wolszczan, A. 1986, *ApJ*, 307, L27  
Cordes, J. M., Wolszczan, A., Dewey, R. J., Blaskiewicz, M., & Stinebring, D. R. 1990, *ApJ*, 349, 245  
Cordes, J. M. & Rickett, B. J. 1998, *ApJ*, 507, 846  
Cordes, J. M., & Lazio, T. J. W. 2002, *arXiv:astro-ph/0207156*  
Cordes, J. M., Kramer, M., Lazio, T. J. W., et al. 2004, *New A Rev.*, 48, 1413  
Cordes, J. M., & Shannon, R. M. 2010, *arXiv:1010.3785*  
Cordes, J. M., Shannon, R. M., & Stinebring, D. R. 2016, *ApJ*, 817, 16  
Cordes, J. M., Wasserman, I., Hessels, J. W. T., et al. 2017, *ApJ*, 842, 35  
Craft, H. D., Jr. 1970, Ph.D. Thesis, Cornell University  
Demorest, P. B. 2007, Ph.D. Thesis, University of California, Berkeley  
Demorest, P. B., Ferdman, R. D., Gonzalez, M. E., et al. 2013, *ApJ*, 762, 94  
Desvignes, G., Caballero, R. N., Lentati, L., et al. 2016, *MNRAS*, 458, 3341  
Donner, J. Y., Verbiest, J. P. W., Tiburzi, C., et al. 2019, *A&A*, in press; *arXiv:1902.03814*  
Dunning, A., Bowen, M., Bourne, M., Hayman, D., & Smith, S. L. 2015. *An ultra-wideband dielectrically loaded quad-ridged feed horn for radio astronomy*. In 2015 IEEE-APS Topical Conference on Antennas and Propagation in Wireless Communications (APWC) (pp. 787-790).  
Fiedler, R. L., Dennison, B., Johnston, K. J., & Hewish, A. 1987, *Nature*, 326, 675  
Fiedler, R., Pauls, T., Johnston, K. J., & Dennison, B. 1994, *ApJ*, 430, 595  
Fonseca, E., Stairs, I. H., & Thorsett, S. E. 2014, *ApJ*, 787, 82  
Foster, R. S., & Cordes, J. M. 1990, *ApJ*, 364, 123

Foster, G., Karastergiou, A., Paulin, R., et al. 2015, *MNRAS*, 453, 1489  
Gentile, P. A., McLaughlin, M. A., Demorest, P. B., et al. 2018, *ApJ*, 862, 47  
Hassall, T. E., Stappers, B. W., Hessels, J. W. T., et al. 2012, *A&A*, 543, A66  
Hewish, A. 1980, *MNRAS*, 192, 799  
Hewish, A., Wolszczan, A., & Graham, D. A. 1985, *MNRAS*, 213, 167  
Hobbs, G., Lyne, A. G., Kramer, M., Martin, C. E., & Jordan, C. 2004, *MNRAS*, 353, 1311  
Howard, T. A., Stovall, K., Dowell, J., Taylor, G. B., & White, S. M. 2016, *ApJ*, 831, 208  
Jones, M. L., McLaughlin, M. A., Lam, M. T., et al. 2017, *ApJ*, 841, 125  
Keith, M. J., Coles, W., Shannon, R. M., et al. 2013, *MNRAS*, 429, 2161  
Lam, M. T., Cordes, J. M., Chatterjee, S., & Dolch, T. 2015, *ApJ*, 801, 130  
Lam, M. T., Cordes, J. M., Chatterjee, S., et al. 2016a, *ApJ*, 819, 155  
Lam, M. T., Cordes, J. M., Chatterjee, S., et al. 2016b, *ApJ*, 821, 66  
Lam, M. T., Cordes, J. M., Chatterjee, S., et al. 2017, *ApJ*, 834, 35  
Lam, M. T. 2017, *Astrophysics Source Code Library*, ascl:1706.011  
Lam, M. T., McLaughlin, M. A., Cordes, J. M., Chatterjee, S., & Lazio, T. J. W. 2018a, *ApJ*, 861, 12  
Lam, M. T., Ellis, J. A., Grillo, G., et al. 2018b, *ApJ*, 861, 132  
Lam, M. T., McLaughlin, M. A., Arzoumanian, Z., et al. 2019, *ApJ*, 872, 193  
Lee, K. J., Bassa, C. G., Janssen, G. H., et al. 2014, *MNRAS*, 441, 2831  
Lentati, L., Shannon, R. M., Coles, W. A., et al. 2016, *MNRAS*, 458, 2161  
Levin, L., McLaughlin, M. A., Jones, G., et al. 2016, *ApJ*, 818, 166  
Lorimer, D. R., & Kramer, M. 2012, *Handbook of Pulsar Astronomy*, by D. R. Lorimer, M. Kramer, Cambridge, UK: Cambridge University Press, 2012  
Madison, D. R., Cordes, J. M., Arzoumanian, Z., et al. 2019, *ApJ*, 872, 150  
Maitia, V., Lestrade, J.-F., & Cognard, I. 2003, *ApJ*, 582, 972  
Manchester, R. N., Hobbs, G., Bailes, M., et al. 2013, *PASA*, 30, e017  
Michilli, D., Hessels, J. W. T., Donner, J. Y., et al. 2018, *MNRAS*, 476, 2704  
Noutsos, A., Sobey, C., Kondratiev, V. I., et al. 2015, *A&A*, 576, A62  
Osłowski, S., van Straten, W., Hobbs, G. B., Bailes, M., & Demorest, P. 2011, *MNRAS*, 418, 1258  
Pennucci, T. T., Demorest, P. B., & Ransom, S. M. 2014, *ApJ*, 790, 93  
Pennucci, T. T. 2015, Ph.D. Thesis, University of Virginia  
Petroff, E., Keith, M. J., Johnston, S., van Straten, W., & Shannon, R. M. 2013, *MNRAS*, 435, 1610  
Phillips, J. A., & Wolszczan, A. 1991, *ApJ*, 382, L27  
Phillips, J. A., & Wolszczan, A. 1992, *ApJ*, 385, 273  
Rankin, J. M., & Roberts, J. A. 1971, *The Crab Nebula*, 46, 114  
Ramachandran, R., Demorest, P., Backer, D. C., Cognard, I., & Lommen, A. 2006, *ApJ*, 645, 303  
Rickett, B. J. 1977, *ARA&A*, 15, 479  
Roberts, J. A., & Ables, J. G. 1982, *MNRAS*, 201, 1119  
Romani, R. W., Blandford, R. D., & Cordes, J. M. 1987, *Nature*, 328, 324  
Savitzky, A., & Golay, M. J. E. 1964, *Anal. Chem.*, 36, 8, 1627-1639  
Shannon, R. M., Osłowski, S., Dai, S., et al. 2014, *MNRAS*, 443, 1463  
Shannon, R. M., Osłowski, S., Dai, S., et al. 2014, *MNRAS*, 443, 1463  
Shannon, R. M., & Cordes, J. M. 2017, *MNRAS*, 464, 2075  
Spangler, S. R., Kavaris, D. W., Kortenkamp, P. S., et al. 2002, *A&A*, 384, 654  
Stinebring, D. R., Cordes, J. M., Rankin, J. M., Weisberg, J. M., & Boriakoff, V. 1984, *ApJS*, 55, 247  
Stinebring, D. R., McLaughlin, M. A., Cordes, J. M., et al. 2001, *ApJ*, 549, L97  
Taylor, J. H. 1992, *Royal Society of London Philosophical Transactions Series A*, 341, 117  
Verbiest, J. P. W., Lentati, L., Hobbs, G., et al. 2016, *MNRAS*, 458, 1267  
You, X. P., Hobbs, G. B., Coles, W. A., Manchester, R. N., & Han, J. L. 2007, *ApJ*, 671, 907